

# Negative capacitance in multidomain ferroelectric superlattices

Pavlo Zubko<sup>1\*</sup>, Jacek C. Wojdel<sup>2\*</sup>, Marios Hadjimichael<sup>1</sup>, Stéphanie Fernandez-Pena<sup>3</sup>, Anaïs Sené<sup>4</sup>, Igor Luk'yanchuk<sup>4,5</sup>, Jean-Marc Triscone<sup>3</sup> & Jorge Íñiguez<sup>2,6</sup>

The stability of spontaneous electrical polarization in ferroelectrics is fundamental to many of their current applications, which range from the simple electric cigarette lighter to non-volatile random access memories<sup>1</sup>. Research on nanoscale ferroelectrics reveals that their behaviour is profoundly different from that in bulk ferroelectrics, which could lead to new phenomena with potential for future devices<sup>2–4</sup>. As ferroelectrics become thinner, maintaining a stable polarization becomes increasingly challenging. On the other hand, intentionally destabilizing this polarization can cause the effective electric permittivity of a ferroelectric to become negative<sup>5</sup>, enabling it to behave as a negative capacitance when integrated in a heterostructure. Negative capacitance has been proposed as a way of overcoming fundamental limitations on the power consumption of field-effect transistors<sup>6</sup>. However, experimental demonstrations of this phenomenon remain contentious<sup>7</sup>. The prevalent interpretations based on homogeneous polarization models are difficult to reconcile with the expected strong tendency for domain formation<sup>8,9</sup>, but the effect of domains on negative capacitance has received little attention<sup>5,10–12</sup>. Here we report negative capacitance in a model system of multidomain ferroelectric–dielectric superlattices across a wide range of temperatures, in both the ferroelectric and paraelectric phases. Using a phenomenological model, we show that domain-wall motion not only gives rise to negative permittivity, but can also enhance, rather than limit, its temperature range. Our first-principles-based atomistic simulations provide detailed microscopic insight into the origin of this phenomenon, identifying the dominant contribution of near-interface layers and paving the way for its future exploitation.

Negative capacitance in ferroelectrics arises from the imperfect screening of the spontaneous polarization<sup>5,10,13,14</sup>. Imperfect screening is intrinsic to semiconductor–ferroelectric, and even metal–ferroelectric, interfaces because of their finite effective screening lengths<sup>15,16</sup>. Alternatively, imperfect screening can be engineered in a controlled manner by deliberately inserting a dielectric layer of relative permittivity  $\epsilon_d$  between the ferroelectric and the electrodes<sup>6</sup> (Fig. 1a). The physical separation of the ferroelectric bound charge from the metallic screening charges creates a depolarizing field inside the ferroelectric, destabilizing the polarization and lowering the ferroelectric transition temperature  $T_C$ . The effect of the dielectric layer can be understood by considering the free energy of the bilayer capacitor with the usual assumption of a uniform polarization  $P$  (see Methods). Below the bulk transition temperature  $T_0$ , the free energy of the ferroelectric layer develops a double-well with minima at finite values of  $P$ , but, when combined with the parabolic potential of the dielectric layer, the total energy has a minimum at  $P=0$  (Fig. 1b). The reciprocal dielectric constant of the system as a whole  $\epsilon^{-1}$ , given by the curvature of the total energy with respect to the polarization, is positive, as required for thermodynamic stability. However, because the non-polar state of the

ferroelectric layer corresponds to a maximum of its local energy, the local stiffness of the ferroelectric layer is negative; that is, polarizing the ferroelectric layer has a negative energy cost.

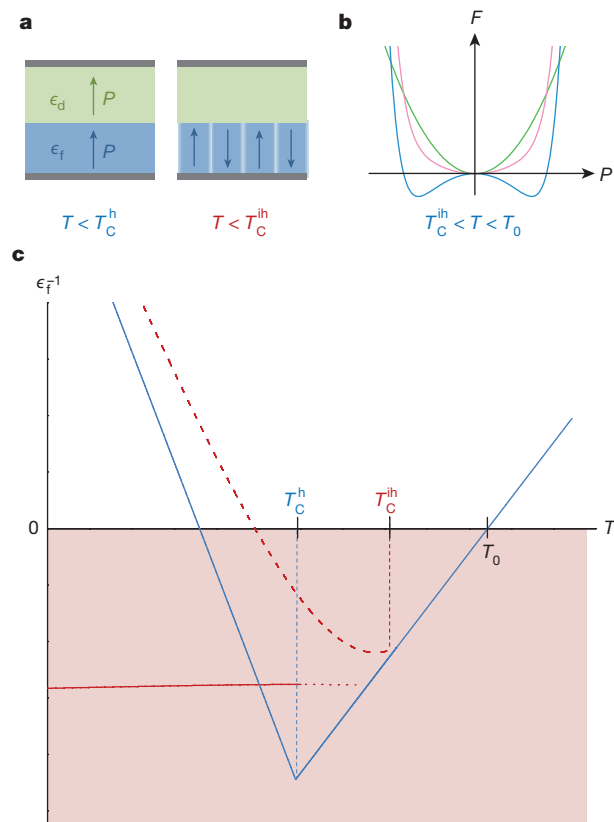


**Figure 1 | Phenomenological description of negative capacitance.** **a**, Sketch of the ferroelectric–dielectric bilayer capacitor with (right) and without (left) domains. Green, blue and grey layers correspond to the dielectric, ferroelectric and metallic components, respectively. **b**, The total (pink) and local free energies  $F$  of the ferroelectric (blue) and dielectric (green) layers. **c**, Temperature  $T$  dependence of the local dielectric stiffness of the ferroelectric layer calculated from phenomenological models with uniform homogeneous polarization (blue), and with inhomogeneous polarization with static, soft domain walls (red, dashed) and mobile, abrupt (thin) domain walls (red, solid). The dotted line marks the breakdown of the thin-wall Landau–Kittel model close to  $T_C$  (see Methods).  $P$ , polarization;  $T_C^h$  and  $T_C^{ih}$ , temperature of ferroelectric transitions to homogeneous and inhomogeneous states, respectively;  $T_0$ , bulk transition temperature;  $\epsilon_d$  and  $\epsilon_f$ , dielectric constants of the dielectric and ferroelectric layers, respectively.

<sup>1</sup>London Centre for Nanotechnology and Department of Physics and Astronomy, University College London, 17–19 Gordon Street, London WC1H 0HA, UK. <sup>2</sup>Institut de Ciència de Materials de Barcelona (ICMAB-CSIC), Campus UAB, 08193 Bellaterra, Spain. <sup>3</sup>Department of Quantum Matter Physics, University of Geneva, CH-1211 Geneva, Switzerland. <sup>4</sup>Laboratory of Condensed Matter Physics, University of Picardie, Amiens 80000, France. <sup>5</sup>L. D. Landau Institute for Theoretical Physics, Moscow, Russia. <sup>6</sup>Materials Research and Technology Department, Luxembourg Institute of Science and Technology (LIST), 5 avenue des Hauts-Fourneaux, L-4362 Esch/Alzette, Luxembourg.

\*These authors contributed equally to this work.

With decreasing temperature, the ferroelectric double-well progressively deepens and would dominate the total energy below a temperature  $T_C^h$ , favouring a transition to a homogeneous ferroelectric state. The local dielectric stiffness of the ferroelectric layer would then increase and eventually become positive, as shown by the blue curve in Fig. 1c. This ‘homogeneous’ model has served as the basis for the interpretation of previous experimental studies of negative capacitance<sup>17–20</sup>. However, although attractively simple, it does not describe the true ground state of the system because, in general, the depolarization field that leads to the negative capacitance effect will also tend to favour a transition to an inhomogeneous, multidomain phase at a temperature  $T_C^{ih}$  ( $T_C^{ih} > T_C^h$ ), as demonstrated by numerous experiments (see, for example, ref. 8). This has consequences for the dielectric response and negative capacitance, as we show with the help of two phenomenological models.

First, we use a Ginzburg–Landau approach (Methods) to obtain an analytic description of the phase transition into an inhomogeneous state with a gradual (soft) polarization profile, typical of ultrathin films<sup>21</sup>. This model allows us to obtain the lattice contribution to the dielectric response (that is, the response of a static domain structure; dashed curve in Fig. 1c). The appearance of the soft domain structure results in qualitative changes in the shape of the  $\epsilon^{-1}(T)$  curve, pushing its minimum below the actual transition temperature. However, the overall effect of a static domain structure is to reduce the temperature range of negative capacitance, as previously thought<sup>11</sup>.

Second, to investigate the contribution of domain-wall motion, we choose to work in the simpler Kittel approximation, which is valid for the abrupt (thin) domain walls typical of thicker films well below  $T_C$  (refs 5, 12, 22). The resulting dielectric response is shown by the solid red curve in Fig. 1c (for details of the calculation, see Methods). Remarkably, domain-wall motion contributes negatively to the overall dielectric stiffness<sup>5,10,12</sup>. Macroscopically, domain-wall displacements create a net polarization that leads to a depolarizing field, which dominates the total field in the ferroelectric, thus leading to negative capacitance. Microscopically, the domain-wall displacements redistribute the interfacial stray fields resulting in a negative net contribution to the free energy and thus to the local dielectric constant. Although the thin-wall Kittel model does not capture the subtleties of the soft domain structure of ultrathin films, it highlights the importance of the contribution of domain walls to extending the temperature window of negative capacitance.

To experimentally access the different temperature regimes of negative capacitance shown in Fig. 1c, we deposited several series of high-quality epitaxial superlattices consisting of  $n_f$  ferroelectric and  $n_d$  dielectric monolayers repeated  $N$  times, hereafter labelled  $(n_f, n_d)_N$ . For each superlattice series,  $n_f$  is fixed while  $n_d$  is varied from four to ten unit cells. SrTiO<sub>3</sub> crystals were used as substrates and epitaxial SrRuO<sub>3</sub> top and bottom electrodes were deposited *in situ* to enable dielectric impedance spectroscopy measurements. SrTiO<sub>3</sub> was also chosen as the dielectric component, and PbTiO<sub>3</sub> and quasi-random Pb<sub>0.5</sub>Sr<sub>0.5</sub>TiO<sub>3</sub> alloys were used as the ferroelectric layers. The Pb<sub>0.5</sub>Sr<sub>0.5</sub>TiO<sub>3</sub> composition was chosen for its low  $T_0$ , enabling us to investigate the full range of temperatures up to and above  $T_0$  without complications arising from leakage.

Such superlattices constitute a model system for the observation of negative capacitance, because they are mathematically equivalent to the bilayer systems investigated theoretically<sup>5,6,21</sup> and present a number of very convenient features—for example, the small layer thicknesses minimize the number of free carriers, ensuring appropriate electrostatic boundary conditions, while the highly ordered stripe domains are well-suited for X-ray diffraction (XRD) studies and theoretical modelling. By varying the thicknesses of the dielectric layers and the total number of bilayer repetitions, the permittivities of the individual layers can be extracted from measurements of the total capacitance of a series of samples.

The dielectric properties of three Pb<sub>0.5</sub>Sr<sub>0.5</sub>TiO<sub>3</sub>–SrTiO<sub>3</sub> superlattices with 14-unit-cell-thick Pb<sub>0.5</sub>Sr<sub>0.5</sub>TiO<sub>3</sub> layers are summarized in Fig. 2a–d. All superlattices exhibit a broad maximum in the dielectric response that moves to lower temperature with increasing SrTiO<sub>3</sub> content (Fig. 2a). These maxima do not coincide with the phase-transition temperature  $T_C^{ih}$  and instead arise from the qualitatively different temperature dependences of the permittivities of the SrTiO<sub>3</sub> and Pb<sub>0.5</sub>Sr<sub>0.5</sub>TiO<sub>3</sub> layers. Using XRD, we obtain an estimate of  $T_C^{ih}$  from the temperature evolution of in-plane and out-of-plane lattice parameters ( $a$  and  $c$ , respectively), as shown in Fig. 2b. Contrary to what is expected for a transition to a homogeneous ferroelectric state, the observed  $T_C^{ih}$  is independent of the thickness of the SrTiO<sub>3</sub> layer because  $T_C^{ih}$  is determined by the domain-wall density, which in turn depends only on the thickness of the ferroelectric layer. The regular domain structure with

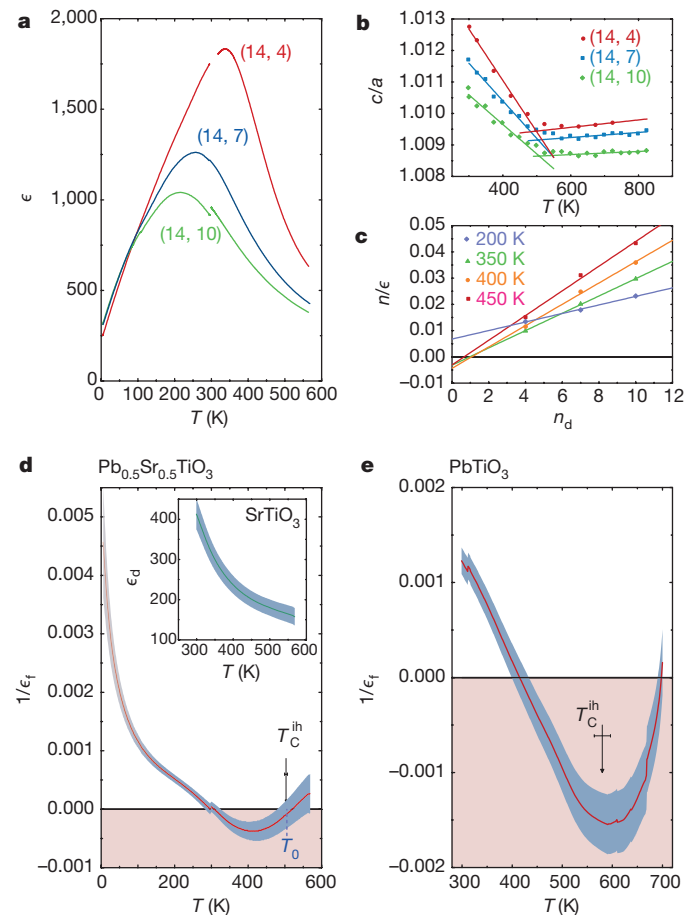


**Figure 2 | Temperature dependence of the dielectric permittivities of Pb<sub>0.5</sub>Sr<sub>0.5</sub>TiO<sub>3</sub>–SrTiO<sub>3</sub> and PbTiO<sub>3</sub>–SrTiO<sub>3</sub> superlattices.** **a**, Total dielectric constant  $\epsilon$  of  $(14, n_d)$  Pb<sub>0.5</sub>Sr<sub>0.5</sub>TiO<sub>3</sub>–SrTiO<sub>3</sub> superlattices as a function of temperature  $T$ . Red,  $n_d = 4$ ; blue,  $n_d = 7$ ; green,  $n_d = 10$ . **b**, Sample tetragonalities  $c/a$  used to determine  $T_C$ . **c**, Linear fits to the series capacitor expression ( $n/\epsilon \approx n_d/\epsilon_d + n_f/\epsilon_f$ , where  $n = n_d + n_f$ ,  $\epsilon_d$  and  $\epsilon_f$  are the dielectric constants of the dielectric and ferroelectric layers, and  $n_d$  and  $n_f$  are the numbers of dielectric and ferroelectric monolayers per period of the superlattice) for a selection of temperatures. **d**, Reciprocal dielectric constant of the Pb<sub>0.5</sub>Sr<sub>0.5</sub>TiO<sub>3</sub> layers in  $(14, n_d)$  superlattices calculated from the series capacitor model. Dashed line indicates our estimate of  $T_0$  obtained from the temperature dependence of  $c/a$  of a thin Pb<sub>0.5</sub>Sr<sub>0.5</sub>TiO<sub>3</sub> film. Inset, dielectric constant of the SrTiO<sub>3</sub> layers. **e**, Reciprocal dielectric constant of the PbTiO<sub>3</sub> layers in  $(5, n_d)$  superlattices. In **d** and **e**, the arrows indicate  $T_C^{ih}$  with associated error bars representing the spread of values between the samples in the series; grey shading indicates estimated uncertainties obtained from weighted-least-squares linear fitting with weights determined from inter-electrode variation at room temperature within each sample.

a periodicity of about 10–12 nm can be observed using XRD as peaks in the diffuse scattering around the superlattice Bragg reflections (Extended Data Fig. 1).

To separate the dielectric constants  $\epsilon_d$  and  $\epsilon_f$  of individual layers we apply the standard series capacitor expression, which for our superlattices is  $n/\epsilon \approx n_d/\epsilon_d + n_f/\epsilon_f$  (see Methods), where  $n = n_d + n_f$  and  $\epsilon$  is the overall dielectric constant of the superlattice, obtained directly from the measured capacitance. The linear relationship between  $n/\epsilon$  and  $n_d$  is well satisfied for  $100 \text{ K} \lesssim T < 570 \text{ K}$ , as illustrated in Fig. 2c for a few selected temperatures. The dielectric constant of the SrTiO<sub>3</sub> layers can be obtained from the slopes of the plots in Fig. 2c. The resulting  $\epsilon_d(T)$  is presented in the inset of Fig. 2d and shows the typical decrease with temperature observed in SrTiO<sub>3</sub> thin films and bulk crystals. The intercepts of the linear plots in Fig. 2c give the reciprocal dielectric constant of the Pb<sub>0.5</sub>Sr<sub>0.5</sub>TiO<sub>3</sub> layers  $\epsilon_f^{-1}$ , which is plotted in Fig. 2d. At low temperature, deep in the ferroelectric regime,  $\epsilon_f^{-1}$  is positive. However, upon heating it slowly decreases, entering the negative capacitance regime around room temperature. It then reaches a minimum, and subsequently returns to positive values at high temperature in the paraelectric phase. The minimum in  $\epsilon_f^{-1}$  is observed well below the phase-transition temperature  $T_C^{\text{th}}$  (indicated with an arrow in Fig. 2d), contrary to what would be expected for a structure with homogeneous polarization. For this series of samples, the temperature regime  $T_C^{\text{th}} < T < T_0$  cannot be resolved because  $T_C^{\text{th}}$  is very close to  $T_0$  (measured independently to be around 500 K for Pb<sub>0.5</sub>Sr<sub>0.5</sub>TiO<sub>3</sub> thin films of the same composition). To access this temperature regime, a set of (5,  $n_d$ )<sub>N</sub> superlattices was fabricated with Pb<sub>0.5</sub>Sr<sub>0.5</sub>TiO<sub>3</sub> replaced by PbTiO<sub>3</sub>, which has a much higher  $T_0 \approx 1,200 \text{ K}$  when grown coherently on SrTiO<sub>3</sub> (ref. 23). As shown in Fig. 2e, the negative capacitance regime can be clearly observed in the paraelectric phase above  $T_C^{\text{th}} \approx 580 \text{ K}$  in these samples. However, above  $T_C$  the dielectric stiffness increases much faster than expected, becoming positive far below  $T_0$ . This is probably due to the progressive increase in the thermally

activated conductivity of the ferroelectric layers, which destroys the electrostatic boundary conditions required for negative capacitance and leads to Maxwell–Wagner relaxations at high temperature (see Methods).

To gain further insight, we used first-principles-based effective models that permit the treatment of thermal effects. We used the potentials for PbTiO<sub>3</sub> and SrTiO<sub>3</sub> introduced in ref. 24 as the starting point to construct models for PbTiO<sub>3</sub>–SrTiO<sub>3</sub> superlattices with an in-plane epitaxial constraint corresponding to a SrTiO<sub>3</sub>(001) substrate (see Methods). As compared with experiment, our models feature relatively stiff SrTiO<sub>3</sub> layers and relatively low ferroelectric transition temperatures; otherwise, they capture the behaviour of PbTiO<sub>3</sub> layers stacked with dielectric layers in a qualitatively and semi-quantitatively correct way. For computational feasibility, we focused on a representative (8, 2) superlattice (10 × 10 × 10 elemental perovskite cells in the periodically repeated simulation box) that presents the behaviour summarized in Fig. 3. As the superlattice is cooled from high temperature, the  $c/a$  ratio of the PbTiO<sub>3</sub> layers (Fig. 3a) evidences an elastic transition, at about 490 K, to a state characterized by strongly fluctuating ferroelectric domains (380-K snapshot provided in Fig. 3d and Supplementary Video 1). This fluctuating phase could be indicative of temperature-induced domain melting, analogous to vortex lattice melting in high-temperature superconductors<sup>25</sup>. As we further cool the superlattice, we observe a ferroelectric transition at 370 K associated with the freezing of the domains into stable stripes. This change can be appreciated in Fig. 3b, in which we plot different measures of the local dipole order inside the PbTiO<sub>3</sub> layer. As shown in the bottom panel of Fig. 3d, this low-temperature phase presents stripes along the [110] direction, with a domain thickness of about five unit cells and sharp walls. As shown in Fig. 3f and Extended Data Fig. 2, in the ground state, the dipoles form closure domains and almost do not penetrate into the stiff SrTiO<sub>3</sub> layers. This corresponds to the vanishing of spontaneous polarization at the surface of a polydomain ferroelectric<sup>26</sup>. The domain

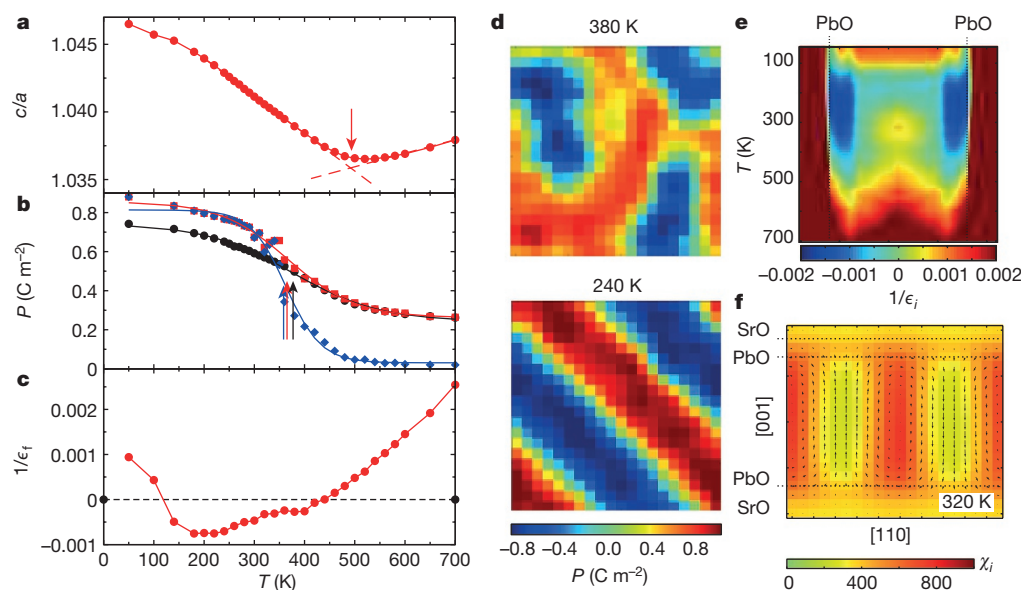


**Figure 3 | Results of Monte Carlo simulations of a first-principles-based model for the (8, 2) superlattice. a–c**, Temperature  $T$  dependence of the tetragonality  $c/a$  (**a**), local polarization  $P$  (**b**) and reciprocal dielectric constant  $1/\epsilon_f$  (**c**) of the PbTiO<sub>3</sub> layer. Solid lines are guides to the eye. **a**, The dashed lines extrapolate the linear behaviour above and below the transition, and help us locate the elastic transition temperature. **b**, Supercell average of the absolute value of the local polarization (black circles), as well as the polarization at a particular cell within a domain considering its absolute (red squares) and bare (blue diamonds) values. The arrow in **a** marks the elastic transition and the onset of

fluctuating polar order around 490 K; those in **b** mark the ferroelectric freezing transition around 370 K as determined from the inflection points. The high-temperature tails of the black and red curves in **b** reveal the presence of incipient polar order. **d**, Snapshots of the local polarization  $P$  (out-of-plane component) within the middle of the PbTiO<sub>3</sub> layer at 380 K (top) and 240 K (bottom). **e**, Temperature dependence of the local dielectric response  $1/\epsilon_f$  resolved along the stacking direction. **f**, Local susceptibility  $\chi_i$  map in the  $(\bar{1}10)$  plane at 320 K. The small arrows represent the projection in the  $(\bar{1}10)$  plane of the local electric dipoles as deduced from the equilibrium atomic configuration.



walls exhibit substantial Bloch character in the ground state; this is the result of a wall-confined polarization along  $[110]$  that appears at about 120 K and is analogous to the one recently predicted<sup>27</sup> for pure  $\text{PbTiO}_3$ .

We investigated the layer-resolved dielectric response of the superlattices. In essence (more details in Methods), we compute the local susceptibility of a region  $i$ ,  $\chi_i = \frac{1}{\epsilon_0} \frac{\partial \langle P_i \rangle}{\partial E_{\text{ext}}}$ , in which  $\epsilon_0$  is the vacuum permittivity,  $P_i$  is the local polarization and  $\langle \dots \rangle$  represents a thermal average that can be readily obtained by simulating our models under an applied electric field  $E_{\text{ext}}$ . As shown in Methods, the local dielectric constant can be expressed as  $\epsilon_i = \epsilon_{\text{tot}} / (\epsilon_{\text{tot}} - \chi_i)$ , where  $\epsilon_{\text{tot}}$  is the dielectric constant of the whole system. The results in Fig. 3c correspond to such a calculation for the  $\text{PbTiO}_3$  layers of the (8, 2) superlattice, and confirm the presence of a region of negative capacitance extending above and below the ferroelectric transition temperature.

However, it is not immediately obvious where the computed negative capacitance comes from. The local susceptibilities  $\chi_i$  are always positive in our calculations, confirming the expectation that an applied external field induces polarization changes that are parallel to it. By contrast, the local dielectric constant  $\epsilon_i$  measures a response to a local field that incorporates depolarizing fields, making its behaviour richer and its physical interpretation more challenging<sup>5</sup>. In particular,  $\epsilon_i$  will be negative if  $\chi_i > \epsilon_{\text{tot}}$ . Hence, the negative capacitance regions are those that are substantially more responsive than the system as a whole.

Our formalism allows us to map out the local response within the  $\text{PbTiO}_3$  layers and thus determine which regions are responsible for the negative capacitance behaviour. Figure 3e shows  $\epsilon_i^{-1}$  resolved along the superlattice-stacking direction and as a function of temperature. At high temperatures, the material behaves like a normal dielectric. Then, negative contributions to  $\epsilon_i^{-1}$  appear at about 550 K, well before any ordering occurs in the system; in that regime, the negative contribution is confined to the vicinity of the  $\text{PbTiO}_3$ - $\text{SrTiO}_3$  interface, and the response of the whole  $\text{PbTiO}_3$  layer continues to be positive. As temperature is further reduced, the negative capacitance region extends to the whole  $\text{PbTiO}_3$  layer. Eventually, at low temperature, the inner part of the  $\text{PbTiO}_3$  layer recovers a conventional dielectric behaviour that dominates the total response, even if our simulations reveal that a negative contribution from the interfaces still persists.

We can further map the susceptibility within the planes perpendicular to the stacking direction to quantify the contributions of domains and domain walls. Figure 3f shows representative results at 320 K. Predictably, we find that the susceptibility at the domain walls is much larger than at the domains. In other words, the field-induced polarization of the walls, which results in the growth or shrinkage of the domains, dominates the response. Further, the large response of the walls is much enhanced in the vicinity of the interfaces with the  $\text{SrTiO}_3$  layers. Hence, our simulations suggest that, below about 370 K, the domain-wall region near the interfaces dominates the negative capacitance of the  $\text{PbTiO}_3$  layers.

There are important differences between our simulated and experimental superlattices that complicate a detailed comparison (see Methods for more details). Nevertheless, our basic result—that the  $\text{PbTiO}_3$  layers have a negative dielectric constant in a temperature region extending above and below  $T_C$ —is confirmed by our simulations. Further, we also ran simulations of various (8,  $n_d$ ) superlattices to mimic our experimental approach for calculating the response of the  $\text{PbTiO}_3$  layer; the results shown in Extended Data Fig. 3 are similar to those of Fig. 3c, thus validating our strategy to measure  $\epsilon_f$ .

Finally, the depolarization effects in ferroelectric-dielectric superlattices are completely analogous to those at interfaces between a ferroelectric and a metal or a semiconductor. We have found that  $\text{PbTiO}_3$ - $\text{SrRuO}_3$  superlattices, for example, exhibit very similar domain structures as  $\text{PbTiO}_3$ - $\text{SrTiO}_3$ . These structures are induced by the imperfect screening at the  $\text{SrRuO}_3$ - $\text{PbTiO}_3$  interfaces, which produces a depolarizing field equivalent to that induced by a 7-unit-cell-thick  $\text{SrTiO}_3$  layer<sup>28,29</sup>. It is therefore reasonable to expect a negative

capacitance effect of the same order of magnitude in a transistor-like structure composed of a  $\text{PbTiO}_3$  gate dielectric and an ultrathin conducting  $\text{SrRuO}_3$  channel, where applying a gate voltage  $V_g$  will lead to an enhancement of the surface potential  $\phi_s$  at the  $\text{PbTiO}_3$ - $\text{SrRuO}_3$  interface. With a  $\text{PbTiO}_3$ - $\text{SrRuO}_3$  interface capacitance  $C_i$  of about  $0.6 \text{ F m}^{-2}$  (ref. 14) and a ferroelectric capacitance  $C_f$  equivalent to that of one of our  $\text{PbTiO}_3$  layers, one can obtain voltage amplification factors  $\frac{\partial \phi_s}{\partial V_g} = \frac{C_f}{C_i + C_f}$  as large as about two at temperatures at which  $\epsilon_f^{-1}$  is most negative. For the more practical interface with a conventional semiconductor, the expected amplification is more modest (for example,  $\frac{\partial \phi_s}{\partial V_g} \approx 1.03$  for  $C_i \approx 0.1 \text{ F m}^{-2}$ , ref. 11), but is still enhanced compared to conventional gate dielectrics for which the corresponding value is less than unity. Such enhancements are especially encouraging in light of recent progress in the integration of ferroelectric oxides directly on conventional semiconductors<sup>30</sup>.

**Online Content** Methods, along with any additional Extended Data display items and Source Data, are available in the online version of the paper; references unique to these sections appear only in the online paper.

**Received 17 July 2015; accepted 8 March 2016.**

**Published online 13 June 2016.**

1. Scott, J. F. & Paz de Araujo, C. A. Ferroelectric memories. *Science* **246**, 1400–1405 (1989).
2. Naumov, I. I., Bellaiche, L. & Fu, H. Unusual phase transitions in ferroelectric nanodisks and nanorods. *Nature* **432**, 737–740 (2004).
3. Garcia, V. *et al.* Giant tunnel electroresistance for non-destructive readout of ferroelectric states. *Nature* **460**, 81–84 (2009).
4. Kim, D. J. *et al.* Ferroelectric tunnel memristor. *Nano Lett.* **12**, 5697–5702 (2012).
5. Bratkovsky, A. M. & Levanyuk, A. P. Very large dielectric response of thin ferroelectric films with the dead layers. *Phys. Rev. B* **63**, 132103 (2001).
6. Salahuddin, S. & Datta, S. Use of negative capacitance to provide voltage amplification for low power nanoscale devices. *Nano Lett.* **8**, 405–410 (2008).
7. Krowne, C. M., Kirchoefer, S. W., Chang, W., Pond, J. M. & Allredge, L. M. B. Examination of the possibility of negative capacitance using ferroelectric materials in solid state electronic devices. *Nano Lett.* **11**, 988–992 (2011).
8. Fong, D. D. *et al.* Ferroelectricity in ultrathin perovskite films. *Science* **304**, 1650–1653 (2004).
9. Catalan, G., Jiménez, D. & Gruverman, A. Ferroelectrics: Negative capacitance detected. *Nat. Mater.* **14**, 137–139 (2015).
10. Bratkovsky, A. M. & Levanyuk, A. P. Depolarizing field and “real” hysteresis loops in nanometer-scale ferroelectric films. *Appl. Phys. Lett.* **89**, 253108 (2006).
11. Cano, A. & Jiménez, D. Multidomain ferroelectricity as a limiting factor for voltage amplification in ferroelectric field-effect transistors. *Appl. Phys. Lett.* **97**, 133509 (2010).
12. Luk'yanchuk, I., Pakhomov, A., Sené, A., Sidorkin, A. & Vinokur, V. Terahertz electrostatics of 180° domain walls in thin ferroelectric films. Preprint at <http://arxiv.org/abs/1410.3124> (2014).
13. Ponomareva, I., Bellaiche, L. & Resta, R. Dielectric anomalies in ferroelectric nanostructures. *Phys. Rev. Lett.* **99**, 227601 (2007).
14. Stengel, M., Vanderbilt, D. & Spaldin, N. A. Enhancement of ferroelectricity at metal-oxide interfaces. *Nat. Mater.* **8**, 392–397 (2009).
15. Mehta, R. R., Silverman, B. D. & Jacobs, J. T. Depolarization fields in thin ferroelectric films. *J. Appl. Phys.* **44**, 3379–3385 (1973).
16. Junquera, J. & Ghosez, P. Critical thickness for ferroelectricity in perovskite ultrathin films. *Nature* **422**, 506–509 (2003).
17. Khan, A. I. *et al.* Experimental evidence of ferroelectric negative capacitance in nanoscale heterostructures. *Appl. Phys. Lett.* **99**, 113501 (2011).
18. Appleby, D. J. R. *et al.* Experimental observation of negative capacitance in ferroelectrics at room temperature. *Nano Lett.* **14**, 3864–3868 (2014).
19. Gao, W. *et al.* Room-temperature negative capacitance in a ferroelectric-dielectric superlattice heterostructure. *Nano Lett.* **14**, 5814–5819 (2014).
20. Khan, A. I. *et al.* Negative capacitance in a ferroelectric capacitor. *Nat. Mater.* **14**, 182–186 (2015).
21. Luk'yanchuk, I. A., Lahoche, L. & Sené, A. Universal properties of ferroelectric domains. *Phys. Rev. Lett.* **102**, 147601 (2009).
22. Kopal, A., Mokry, P., Fousek, J. & Bahnik, T. Displacements of 180° domain walls in electroded ferroelectric single crystals: the effect of surface layers on restoring force. *Ferroelectrics* **223**, 127–134 (1999).
23. Dawber, M. *et al.* Tailoring the properties of artificially layered ferroelectric superlattices. *Adv. Mater.* **19**, 4153–4159 (2007).
24. Wojdeł, J. C., Hermet, P., Ljungberg, M. P., Ghosez, P. & Íñiguez, J. First-principles model potentials for lattice-dynamical studies: general methodology and example of application to ferroic perovskite oxides. *J. Phys. Condens. Matter* **25**, 305401 (2013).

25. Blatter, G., Feigel'man, M. V., Geshkenbein, V. B., Larkin, A. I. & Vinokur, V. M. Vortices in high-temperature superconductors. *Rev. Mod. Phys.* **66**, 1125–1388 (1994).
26. De Guerville, F., Luk'yanchuk, I., Lahoche, L. & El Marssi, M. Modeling of ferroelectric domains in thin films and superlattices. *Mater. Sci. Eng. B* **120**, 16–20 (2005).
27. Wojdel, J. C. & Íñiguez, J. Ferroelectric transitions at ferroelectric domain walls found from first principles. *Phys. Rev. Lett.* **112**, 247603 (2014).
28. Lichtensteiger, C., Fernandez-Pena, S., Weymann, C., Zubko, P. & Triscone, J.-M. Tuning of the depolarization field and nanodomain structure in ferroelectric thin films. *Nano Lett.* **14**, 4205–4211 (2014).
29. Aguado-Puente, P. & Junquera, J. Ferromagneticlike closure domains in ferroelectric ultrathin films: first-principles simulations. *Phys. Rev. Lett.* **100**, 177601 (2008).
30. Warusawithana, M. P. *et al.* A ferroelectric oxide made directly on silicon. *Science* **324**, 367–370 (2009).

**Supplementary Information** is available in the online version of the paper.

**Acknowledgements** We acknowledge financial support from the EPSRC (Grant No. EP/M007073/1; P.Z. and M.H.), the A. G. Leventis Foundation (M.H.); FNR Luxembourg (Grant No. FNR/P12/4853155/Kreisel; J.I.), MINECO-Spain (Grant No. MAT2013-40581-P; J.I. and J.C.W.), the Swiss National Science Foundation Division II (J.-M.T. and S.F.-P.), the European Research Council under the European Union's Seventh Framework Programme (FP7/2007-2013)/ERC (Grant No. 319286 (Q-MAC); J.-M.T. and S.F.-P.), and the EU-FP7-ITN project NOTEDEV (Grant No. 607521; I.L.).

**Author Contributions** P.Z., M.H., S.F.-P. and J.-M.T. performed and analysed the experiments. A.S. and I.L. developed the phenomenological theory. J.C.W. and J.I. developed the atomistic models and performed the simulations.

**Author Information** Reprints and permissions information is available at [www.nature.com/reprints](http://www.nature.com/reprints). The authors declare no competing financial interests. Readers are welcome to comment on the online version of the paper. Correspondence and requests for materials should be addressed to P.Z. ([p.zubko@ucl.ac.uk](mailto:p.zubko@ucl.ac.uk)) or J.I. ([jorge.iniguez@list.lu](mailto:jorge.iniguez@list.lu)).

## METHODS

**Landau theory for monodomain bilayers and superlattices.** To derive the expected temperature dependence of the dielectric function of a ferroelectric–dielectric bilayer or superlattice undergoing a phase transition to a homogenous (monodomain) state, we consider the free energy of the bilayer capacitor under short-circuit boundary conditions (or equivalently, one period of a superlattice) of the form

$$F = l_f \left( \frac{\alpha_f}{2} P^2 + \frac{\beta_f}{4} P^4 + \frac{\epsilon_0}{2} E_f^2 \right) + l_d \frac{\epsilon_0 \epsilon_d}{2} E_d^2 \quad (1)$$

The first term represents the energy density, per unit area, of a ferroelectric material with a second-order phase transition at a temperature  $T_0$  as determined by the coefficient of the  $P^2$  term,  $\alpha_f = (T - T_0)/(C\epsilon_0)$ . The second term describes the energy penalty for polarizing the dielectric layer with dielectric constant  $\epsilon_d$ . Here  $E_f$  and  $E_d$  are the electric fields appearing in the ferroelectric and dielectric layers, respectively, when the spontaneous polarization  $P$  develops,  $C$  is the Curie constant,  $\beta_f$  is the coefficient of the  $P^4$  term and  $l_{d,f}$  are the thicknesses of the dielectric and ferroelectric layers respectively. Taking into account the electrostatic boundary conditions at the ferroelectric–dielectric interface,  $\epsilon_d \epsilon_0 E_d = \epsilon_0 E_f + P$ , and the short-circuit condition for the whole system,  $l_d E_d + l_f E_f = 0$ , the functional in equation (1) can be rewritten in terms of only  $P$  with a renormalized overall  $P^2$  coefficient and the corresponding lowering of the transition temperature. The transition to a homogeneous ferroelectric state is thus predicted to occur at a temperature

$$T_C^h = T_0 - C \left( 1 + \frac{l_f}{l_d} \epsilon_d \right)^{-1}$$

In particular, when  $\epsilon_d \gg 1$  and  $l_d$  is of the order of  $l_f$ , equation (1) reduces to

$$F \approx l_f \left( \frac{\alpha_f}{2} P^2 + \frac{\beta_f}{4} P^4 \right) + l_d \left( \frac{1}{2\epsilon_0 \epsilon_d} P^2 \right)$$

which describes the energy of a homogeneously polarized bilayer with equal polarizations in both layers<sup>17,23</sup>.  $T_C^h$  then simplifies to

$$T_C^h \approx T_0 - \frac{l_d}{l_f \epsilon_d} C$$

The overall electric susceptibility  $\chi$  of such a system is given by

$$\frac{l}{\chi} = \epsilon_0 \frac{\partial^2 F}{\partial P^2} = \frac{l_d}{\chi_d} + \frac{l_f}{\chi_f}$$

where  $l = l_f + l_d$ , and  $\chi_d \approx \epsilon_d$  and  $\chi_f = (\alpha_f + 3\beta_f P^2)^{-1} \epsilon_0^{-1}$  are the electric susceptibilities of the dielectric and ferroelectric layers, respectively. It has the familiar form of the series capacitance formula,  $1/C_{\text{tot}} = 1/C_d + 1/C_f$ . For high permittivity materials such as those considered in this work,  $\chi = \epsilon$  is a very good approximation. The temperature dependence of the contribution to the reciprocal dielectric constant from the ferroelectric layer is shown in Fig. 1c (blue curve). Although the total permittivity (not shown) exhibits the typical divergence ( $\epsilon^{-1} = 0$ ) at  $T_C^h$  and is always positive, as required for thermodynamic stability, the dielectric stiffness of the ferroelectric component decreases linearly with temperature upon cooling and acquires negative values below  $T_0$ . At  $T_C^h$ , the spontaneous polarization appears and the  $3\beta_f P^2$  term eventually restores  $\epsilon_f^{-1}$  to positive values at lower temperatures. To obtain the blue curve in Fig. 1c, we modelled a 30-nm-thick PbTiO<sub>3</sub> film in series with a 10-nm-thick SrTiO<sub>3</sub> layer using the following parameters:  $T_0 = 1,244$  K (strain-renormalized),  $C = 4.1 \times 10^5$  K and  $\epsilon_d = 300$ , giving  $T_C^h = 788$  K.

**Landau–Kittel model of domain-wall contribution to permittivity.** For an isolated ferroelectric slab of thickness  $l_f$  in zero applied field, the up- and down-oriented 180° domains are of equal width  $w$ , given by the Landau–Kittel square-root dependence<sup>31,32</sup>. For high- $\epsilon$  ferroelectrics

$$w \approx \left( \frac{\epsilon_{\perp}}{\epsilon_{\parallel}} \right)^{\frac{1}{4}} \sqrt{\zeta \times \lambda \times 2\xi \times l_f}$$

where  $\epsilon_{\parallel}$  and  $\epsilon_{\perp}$  are the ‘bulk’ lattice dielectric constants parallel and perpendicular to the polarization, respectively,  $\xi$  is the coherence length,  $\lambda = 1 + \epsilon_d/(\epsilon_{\parallel}\epsilon_{\perp})^{1/2}$  and  $\zeta \approx 3.53$  (refs 5, 12, 26, 33, 34). This equation also holds for ferroelectric films with ‘dead layers’ and ferroelectric–dielectric superlattices, provided that the dielectric layers are thick enough compared to the domain width to allow the interfacial stray fields to decay sufficiently. Upon application of a field, the ferroelectric layer develops a net polarization due to the dielectric response of the lattice, described by  $\epsilon_{\parallel}$ , and to the motion of domain walls. To calculate the domain-wall contribution,

one must find the field-induced changes to the stray depolarizing fields, as has been done in refs 5, 12, 22. The resulting effective dielectric constant of the ferroelectric can be expressed as<sup>12</sup>

$$\epsilon_f = \epsilon_{\parallel} - \frac{\pi}{4\ln(2)} \sqrt{\frac{\epsilon_{\perp}}{\epsilon_{\parallel}}} \frac{l_f}{w} \lambda \epsilon_{\parallel}$$

where the first term is the lattice response and the second term is the negative contribution from domain-wall motion. Within the limits of the validity of the Landau–Kittel theory,  $l_f/w$  is large and therefore the second term is dominant. This term originates from the field-induced changes in the inhomogeneous electric-field distribution at the interface between the ferroelectric and the dielectric layers, consistent with the findings of our atomistic calculations.

The temperature dependence of  $w$  and  $\epsilon_f$  can be estimated<sup>35</sup> using the standard critical Ginzburg–Landau expansions near  $T_0$

$$\xi(T) = \frac{\xi_0}{(1 - T/T_0)^{1/2}}; \quad \epsilon_{\parallel}(T) = \frac{1}{2} \frac{\kappa_{\parallel}}{1 - T/T_0} \quad (2)$$

where  $\kappa_{\parallel}$  is related to the Curie constant  $C$  via  $\kappa_{\parallel} = C/T_0$  and  $\xi_0$  is the atomic-scale coherence length at  $T = 0$ . Assuming that  $\epsilon_{\perp}$  is temperature independent, the domain width  $w$  is almost temperature independent<sup>21,26</sup>, whereas the approximate temperature dependence of  $\epsilon_f$  is sketched in Fig. 1c. The solid red curve in Fig. 1c was calculated for a 30-nm-thick film with the following parameters (corresponding roughly to those of strained PbTiO<sub>3</sub>):  $T_0 = 1,244$  K,  $C = 4.1 \times 10^5$  K,  $\epsilon_{\perp} = 120$  and  $2\xi_0 = 1$  nm.

**Ginzburg–Landau theory of polydomain bilayers and superlattices.** The critical temperature of transition to the inhomogeneous striped domain state can be calculated within Ginzburg–Landau theory<sup>26,33</sup>

$$T_C^h = (1 - \pi\tau) T_0$$

where  $\tau = (C/T_0\epsilon_{\perp})^{1/2} \times 2\xi_0/l_f$ . For a 30-nm-thick PbTiO<sub>3</sub> film, we obtain  $T_C^h \approx 1,030$  K. A similar expression (up to a numerical factor) can be obtained on the qualitative level by noting that, at  $T_C^h$ , the domain width  $w$  becomes comparable with the domain-wall thickness  $2\xi(T)$ .

Close to  $T_C^h$ , the Landau–Kittel thin-wall approximation breaks down as the domain profile becomes soft (we represent this region by the dotted line in Fig. 1c). The theory for mobile domain walls in this regime is challenging, but the lattice part of the response of the polydomain structure can be calculated analytically. This would correspond to a situation in which domain-wall motion is impeded, for instance, by pinning of the domain walls. Using Ginzburg–Landau theory, this contribution can be expressed as<sup>35</sup>

$$\epsilon_f(T) = \frac{2\epsilon_{\parallel}(T)}{3\langle P^2 \rangle / P_B^2 - 1}$$

which is a generalization of equation (2). Here,  $P_B = P_0(1 - T/T_0)^{1/2}$  is the normalized temperature-dependent polarization of the bulk short-circuited sample and  $\langle P^2 \rangle = \langle P^2(x, y) \rangle$  is the spatial average of the temperature-dependent polarization profile of the domain state with critical temperature  $T_C^h$ . The factor  $\langle P^2 \rangle$  can be calculated over a wide temperature interval that includes both soft and abrupt (thin) domain profiles using the universal expression for  $P(x, y)$  in terms of elliptic sn functions, as given in equation (7) of ref. 21. After spatially averaging we obtain

$$\epsilon_{f, \text{GL}}^{-1}(T) = \frac{T_0}{C} \left( \frac{T}{T_0} - 1 \right) \left[ 1 - 3F \left( 1 - \frac{T}{T_C^h} \right) \right], \quad T < T_C^h$$

where  $F(x) = [K(m(x)) - E(m(x))]^2 / m^2 \times \tanh(0.357\tau x)$ ,  $K(m)$  and  $E(m)$  are the complete elliptic integrals of the first and second kind, respectively, with  $m(x) \approx \tanh(0.27\tau x)$  and  $\tau = (C/T_0\epsilon_{\perp})^{1/2} \times 2\xi_0/l_f$ . Note that  $F(0) = 0$  and that the above expression matches the relative permittivity of the paraelectric state  $\epsilon_p(T) = C/(T - T_0)$  at  $T = T_C^h$ . The temperature dependence of  $\epsilon_{f, \text{GL}}^{-1}$  is shown by the dashed red line in Fig. 1c.

**Sample preparation.** Superlattices were deposited on monocrystalline SrTiO<sub>3</sub>(100) substrates using off-axis radiofrequency magnetron sputtering. PbTiO<sub>3</sub> and SrTiO<sub>3</sub> were deposited at a substrate temperature of 520 °C in an O<sub>2</sub>/Ar mixture of ratio 5/7 and total pressure of 180 mTorr. For SrRuO<sub>3</sub> layers, acting as top and bottom electrodes, the corresponding parameters were 635 °C, 1/20 and 100 mTorr. Pb<sub>0.5</sub>Sr<sub>0.5</sub>TiO<sub>3</sub> layers were deposited by sequential sputtering of sub-monolayer amounts of SrTiO<sub>3</sub> and PbTiO<sub>3</sub>. The Pb<sub>0.5</sub>Sr<sub>0.5</sub>TiO<sub>3</sub>–SrTiO<sub>3</sub> superlattices were asymmetrically terminated with bottom SrRuO<sub>3</sub>–Pb<sub>0.5</sub>Sr<sub>0.5</sub>TiO<sub>3</sub> and top SrTiO<sub>3</sub>–SrRuO<sub>3</sub> interfaces. By contrast, the PbTiO<sub>3</sub>–SrTiO<sub>3</sub> superlattices were



symmetrically terminated with both metal–insulator interfaces being between SrTiO<sub>3</sub> and SrRuO<sub>3</sub>; the thickness of interfacial SrTiO<sub>3</sub> layers was chosen to be half of those in the superlattice interior to maintain a constant overall composition. For each series of superlattices, the thickness of the ferroelectric layers was fixed (14 unit cells for Pb<sub>0.5</sub>Sr<sub>0.5</sub>TiO<sub>3</sub> and 5 unit cells for PbTiO<sub>3</sub>), whereas the thickness of the SrTiO<sub>3</sub> layers was varied from 4 unit cells to 10 unit cells. The number of repetitions  $N$  was chosen to maintain the total superlattice thickness as close as possible to 100 nm for PbTiO<sub>3</sub>–SrTiO<sub>3</sub> superlattices and 200 nm for Pb<sub>0.5</sub>Sr<sub>0.5</sub>TiO<sub>3</sub>–SrTiO<sub>3</sub> superlattices. To extract the interface capacitance contribution, a series of (5, 8)<sub>*N*</sub> PbTiO<sub>3</sub>–SrTiO<sub>3</sub> superlattices with  $N = 10, 19$  and 30 was used.

The top SrRuO<sub>3</sub> layers were patterned using ultraviolet photolithography and etched using an Ar ion beam to form a series of 240 μm × 240 μm capacitors. Structural characterization was performed using a PANalytical X'Pert PRO diffractometer equipped with a triple axis detector and an Anton Paar domed heating stage. Dielectric impedance spectroscopy in the 100-Hz to 2-MHz frequency range was performed using an Agilent E4980A Precision LCR meter in a tube furnace with a custom-made sample holder under continuous O<sub>2</sub> flow at atmospheric pressure.

**Structural analysis.** Specular  $\theta$ – $2\theta$  scans were used to determine the periodicity of the superlattice (Extended Data Fig. 1a), whereas rocking curves were used to confirm the presence of domains and determine their periodicity (Extended Data Fig. 1b, c). Temperature evolution of the lattice parameters was obtained from  $\theta$ – $2\theta$  scans and used to determine the phase-transition temperatures, taken to be the crossing point of linear fits to the high and low temperature data (see Fig. 2b). **Calculation of the permittivities of the individual layers.** The total measured capacitance of the sample  $C_{\text{tot}}$  has contributions from the superlattice  $C_{\text{SL}}$  and the two metal–dielectric interfaces  $C_i$

$$\frac{1}{C_{\text{tot}}} = \frac{1}{C_{\text{SL}}} + \frac{2}{C_i} = \frac{1}{C_f} + \frac{1}{C_d} + \frac{2}{C_i}$$

where  $C_f$  and  $C_d$  are the total (series) capacitances of all the ferroelectric (PbTiO<sub>3</sub>) and dielectric (SrTiO<sub>3</sub>) layers, respectively. For an ( $n_f, n_d$ )<sub>*N*</sub> superlattice

$$\frac{d}{\epsilon} = \frac{d_d}{\epsilon_d} + \frac{d_f}{\epsilon_f} + \frac{2}{\tilde{C}_i}$$

$$\frac{N(n_f + n_d) \tilde{\epsilon}}{\epsilon} = \frac{Nn_d c_d}{\epsilon_d} + \frac{Nn_f c_f}{\epsilon_f} + \frac{2}{\tilde{C}_i}$$

where  $\tilde{C}_i = C_i/(e_0 A)$ ,  $A$  is the sample area,  $d_{d,f}$  are the total thicknesses of the dielectric and ferroelectric components, respectively,  $d = d_d + d_f$  and  $c_{d,f}$  are the lattice constants of the dielectric and ferroelectric layers, respectively. Because  $c_f \approx c_d \approx \tilde{\epsilon} \equiv (n_d c_d + n_f c_f)/(n_d + n_f)$

$$\frac{n_d + n_f}{\epsilon} \equiv \frac{n}{\epsilon} \approx \frac{n_d}{\epsilon_d} + \frac{n_f}{\epsilon_f} + \frac{2}{N\tilde{\epsilon}\tilde{C}_i}$$

For a series of superlattices with a fixed  $n_f$  and  $n_d$ , but varying  $N$ , the interfacial contribution  $1/(\tilde{\epsilon}\tilde{C}_i)$  can be obtained from the slope of a plot of  $n/\epsilon$  versus  $1/N$ . Once the temperature dependence of the interfacial capacitance is known, the permittivities of the individual SrTiO<sub>3</sub> and PbTiO<sub>3</sub> layers can be obtained, using a series of samples with fixed  $n_f$  and varying  $n_d$ , from the slope and intercept of the plot of  $n/\epsilon - 2/(N\tilde{\epsilon}\tilde{C}_i)$  versus  $n_d$ .

This analysis relies on the assumption that the layer permittivities do not change as the thicknesses of the individual layers are varied within each superlattice series. It is therefore crucial that the thickness of the ferroelectric layers is held fixed, because it determines the periodicity of the ferroelectric domain structure and thus the ferroelectric transition temperature and the domain-wall contribution to the measured dielectric constant. All superlattices within a series must also be in the same regime of electrostatic coupling, which places a lower limit on the thickness of the SrTiO<sub>3</sub> layers of around 3–4 unit cells<sup>36</sup>.

To quantify the interface contribution  $C_i$  for the PbTiO<sub>3</sub>-based superlattices, a series of symmetrically terminated samples with a fixed period (5, 8)<sub>*N*</sub>, but varying number of repetitions  $N$ , was fabricated. The interface capacitance was extracted from the intercept of the plot of  $n/\epsilon$  versus  $1/N$ , as discussed above, and is shown as a function of temperature in Extended Data Fig. 4. At room temperature,  $C_i$  is around 1,000 fF μm<sup>-2</sup>, which is in excellent agreement with previous experimental work<sup>37</sup> and compares quite well with the density functional theory prediction of 615 fF μm<sup>-2</sup> at 0 K for the same interface<sup>38</sup>. The weak dependence of  $C_i$  on temperature is also consistent with previous reports<sup>37</sup>. Quantifying the interfacial contribution independently in this way allows us to extract the temperature range of the negative capacitance regime more reliably. As illustrated in Extended Data Fig. 4, the interfacial contribution does not change the qualitative behaviour of the extracted PbTiO<sub>3</sub> dielectric constant and makes only a small (within error bars)

difference to the extracted PbTiO<sub>3</sub> stiffness. It is thus reasonable to neglect this correction, as was done in Fig. 2.

**Impedance analysis.** The observation of negative capacitance relies on the electrostatic interactions between the ferroelectric and dielectric layers, which in turn require both materials to be sufficiently insulating to avoid the screening of the spontaneous polarization. To identify the origin of dielectric losses and to quantify the conductivity of our samples, we measured complex impedance spectra over a wide range of frequencies from 100 Hz to 2 MHz and performed equivalent-circuit modelling. We present the complex impedance  $Z(\omega) = Z' + iZ''$  (in which  $\omega$  is the angular frequency,  $Z' = \text{Re}(Z)$  and  $Z'' = \text{Im}(Z)$ ) data in the complex capacitance representation  $C(\omega) = C' + iC'' \equiv 1/[i\omega Z(\omega)]$  (with  $C' = \text{Re}(C)$  and  $C'' = \text{Im}(C)$ ) as is common for capacitive systems.

Each PbTiO<sub>3</sub> and SrTiO<sub>3</sub> layer in the superlattice, as well as the two metal–dielectric interfaces, can be considered as a parallel R–C element, with a capacitance  $C_j$  and a resistance  $R_j$  due to the finite conductivity of the layer. The superlattice is then modelled by connecting these R–C elements in series, as shown in the inset of Extended Data Fig. 5. An additional series resistance  $R_s$  (typically a few hundred ohms) accounts for the contact resistances and other sources of resistance in the external circuit.

At low temperature, the conductivities of the PbTiO<sub>3</sub> and SrTiO<sub>3</sub> layers are negligible and the whole system behaves as a single capacitance  $C = (\sum_j C_j^{-1})^{-1}$ . The measured  $C'$  is frequency independent except for the high-frequency roll-off due to the parasitic series resistance  $R_s$ . As shown in Extended Data Fig. 5 for a (5, 8)<sub>30</sub> PbTiO<sub>3</sub>–SrTiO<sub>3</sub> superlattice, even at 500 K, the data can be well modelled by a single capacitor in series with  $R_s$ ; the parallel resistance is too high to be determined from the fit (that is, well above 10<sup>8</sup> Ω). At higher temperatures, the superlattice conductivity increases resulting in an increase in the dielectric loss  $C''$  at low frequencies. The 600-K data are modelled with one parallel R–C element in series with  $R_s$ . Despite the high temperature and large electrode area (240 μm × 240 μm), the total sample resistance is still 2 MΩ. However, at 700 K, the total sample resistance drops to 8.8 kΩ. In addition, some layers become substantially more conducting than others, giving rise to Maxwell–Wagner relaxations<sup>39</sup>, which can be observed as steps and plateaus in  $C'(\omega)$ . The behaviour can be qualitatively captured by dividing the system into two blocks with different resistances, each modelled as a parallel R–C element. However, to reproduce the more gradual frequency dispersion, more R–C elements are needed (in this case three were sufficient). At these temperatures, the samples are too conducting to maintain the electrostatic conditions necessary for negative capacitance. The sample resistances for all data shown in Fig. 2 were higher than 1 MΩ.

**Atomistic simulations of PbTiO<sub>3</sub>–SrTiO<sub>3</sub> superlattices.** To construct the first-principles models for the PbTiO<sub>3</sub>–SrTiO<sub>3</sub> superlattices, we took advantage of previously introduced<sup>24</sup> potentials for the bulk compounds, which give a qualitatively correct description of the lattice-dynamical properties and structural phase transitions of both materials. Then, we treated the interface between PbTiO<sub>3</sub> and SrTiO<sub>3</sub> in an approximate way, relying on the following observations. (1) The inter-atomic force constants in perovskite oxides such as PbTiO<sub>3</sub> and SrTiO<sub>3</sub> have been shown to depend strongly on the identity of the involved chemical species and weakly on the chemical environment<sup>40</sup>. (Hence, for example, the interactions between Ti and O are very similar in both PbTiO<sub>3</sub> and SrTiO<sub>3</sub>.) (2) Except in the limit of very-short-period superlattices, the main effects of the stacking are purely electrostatic and largely independent of the details of the interactions at the interfaces. (3) The main purely interfacial effects leading, for example, to the occurrence of new orders (such as those discussed in ref. 41) are related to the symmetry breaking, which permits new couplings that are forbidden by symmetry in the bulk case. Such qualitative symmetry-breaking effects are trivially captured by our potentials, even if the actual values of the interactions are approximate. (Similar approaches to treat ferroelectric superlattices and junctions can be found in the literature, ref. 42 being a representative case.)

As a result of these approximations, we were able to construct our superlattice potentials by using the models for bulk PbTiO<sub>3</sub> and SrTiO<sub>3</sub> to describe the interactions within the layers, assuming a simple numerical average for the interactions of the ion pairs touching or crossing the interface. For example, Ti–O interactions in a TiO<sub>2</sub> interface plane are computed as the average of the analogous Ti–O interactions in PbTiO<sub>3</sub> and SrTiO<sub>3</sub>. New interactions, such as those involving Pb and Sr neighbours across the interface, are chosen so that the acoustic sum rules are respected; in practice, their values are close to an average between the analogous Sr–Sr and Pb–Pb pairs. Finally, the long-range dipole–dipole interactions are governed by a bare electronic dielectric constant  $\epsilon_\infty$  that is taken as a weighted average of the first-principles results for bulk PbTiO<sub>3</sub> (8.5 $\epsilon_0$ ) and SrTiO<sub>3</sub> (6.2 $\epsilon_0$ ), with weights reflecting the composition of the superlattice.

The parameters of our models for bulk PbTiO<sub>3</sub> and SrTiO<sub>3</sub> were computed from first principles as described in ref. 24. To model our PbTiO<sub>3</sub>–SrTiO<sub>3</sub> superlattices, we adjusted our models in the following ways. (1) We softened the model for

bulk SrTiO<sub>3</sub> so that it has a dielectric permittivity  $\epsilon_{33}$  of about  $300\epsilon_0$  at room temperature. We checked *a posteriori* that the SrTiO<sub>3</sub> layers in the superlattices are not as soft, which is probably a consequence of the modified electrostatic interactions ( $\epsilon_\infty$ ) assumed, as described above. (2) We imposed an epitaxial constraint corresponding to having a SrTiO<sub>3</sub> (001)-oriented substrate; that is, we assume in-plane lattice constants  $a = b = 3.901 \text{ \AA}$ , forming an angle  $\gamma = 90^\circ$ . (3) We tweaked the model for PbTiO<sub>3</sub> so that it gives an out-of-plane polarization of  $1.0 \text{ C m}^{-2}$  at 0 K when subject to the epitaxial constraint just described. Care was needed because the model of ref. 24 for bulk PbTiO<sub>3</sub> becomes unstable when the epitaxial constraint is used in combination with the change in  $\epsilon_\infty$ . Nevertheless, it was possible to obtain a stable model with the correct ground-state polarization by adjusting the expansive hydrostatic pressure introduced in ref. 24 as an empirical correction: instead of the  $-13.9 \text{ GPa}$  used in ref. 24, here we used  $-11.2 \text{ GPa}$ . Also, when we use this model to simulate a film of PbTiO<sub>3</sub> under the SrTiO<sub>3</sub> epitaxial constraint, we get a ferroelectric transition temperature of  $460 \text{ K}$ , which is slightly below the temperature at which the fluctuating domains appear in the (8, 2) superlattice ( $490 \text{ K}$ ). As in the case of SrTiO<sub>3</sub>, the difference between bulk material and superlattice is probably caused by the different value of  $\epsilon_\infty$ : we use a slightly larger value for the pure film, which results in a weaker ferroelectric instability.

These approximations and adjustments allow us to construct models for superlattices of arbitrary ( $n_b, n_a$ ) stacking. For the simulations, we used periodically repeated supercells that contain  $10 \times 10$  elemental perovskite units in-plane, whereas out-of-plane they expand one full superlattice period. Thus, for example, for the (8, 2) superlattice, we used a simulation box that contains  $10 \times 10 \times (8 + 2) \times 5 = 5,000$  atoms. We solved the models by running Monte Carlo simulations comprising between 10,000 and 40,000 thermalization sweeps (longer thermalization is needed in the vicinity of phase transitions) followed by 50,000 sweeps to compute thermal averages. The dielectric susceptibility was calculated by applying a small out-of-plane electric field to the simulation box. We found that, in this highly reactive system, this approach converged much faster than the usual fluctuation formulas<sup>43</sup>.

The low-temperature ground state of our (8, 2) superlattice is sketched in Extended Data Fig. 2, in which the stripe domain structure can be nicely appreciated. This result closely resembles the one obtained directly from first-principles calculations<sup>44</sup> in the limit of 0 K; this agreement further confirms the accuracy of our model potential.

**Calculation of local dielectric constants.** In the following, we summarize the derivation of formulas that relate the local response of each layer with the global response of the superlattice. Here we are exclusively concerned with the response along the superlattice stacking direction. We use a '0' superscript to refer to the situation in which no external electric field is applied, and  $i$  to label the layers in the superlattice. In absence of free charges, the condition on the continuity of the electric displacement implies

$$D_i^0 = D^0 = P_i^0 + \epsilon_0 E_i^0$$

for all layers.  $E_i^0$  is the total electric field acting on layer  $i$ . In general, this total field can be split into local and external contributions, so that  $E_i = E_{i,\text{loc}} + E_{\text{ext}}$ . Naturally, when no external field is applied, we simply have  $E_i^0 = E_{i,\text{loc}}^0$ .

Additionally, if we have  $M$  layers in the repeated unit of the superlattice, the periodicity of the potential implies that

$$\sum_{i=1}^M l_i E_i^0 = 0$$

in which  $l_i$  is the thickness of layer  $i$ . Hence, in the absence of an applied field, there is no net potential drop across the supercell. Then, we immediately get that

$$D^0 = L^{-1} \sum_{i=1}^M l_i D_i^0 = L^{-1} \sum_{i=1}^M l_i P_i^0 = P^0$$

in which  $L = \sum_{i=1}^M l_i$  is one superlattice period and  $P^0$  is the polarization of the superlattice with no field applied. As a result, the electric field at layer  $i$  is

$$E_i^0 = E_{i,\text{loc}}^0 = (P^0 - P_i^0) / \epsilon_0$$

Now we consider an external electric field  $E_{\text{ext}}$ . It is trivial to verify that the field-induced variations in polarization, electric field and displacement satisfy

$$\Delta D_i = \Delta D = \Delta P_i + \epsilon_0 (\Delta E_{i,\text{loc}} + E_{\text{ext}}) = \Delta P + \epsilon_0 E_{\text{ext}}$$

$$\sum_{i=1}^M l_i \Delta E_{i,\text{loc}} = 0$$

and

$$\Delta E_{i,\text{loc}} = (\Delta P - \Delta P_i) / \epsilon_0$$

Then, the dielectric constant of layer  $i$  is computed as

$$\epsilon_i = \frac{\Delta D}{\epsilon_0 \Delta E_i} = \frac{(\Delta P + \epsilon_0 E_{\text{ext}})}{\Delta P - \Delta P_i + \epsilon_0 E_{\text{ext}}} = \frac{(\chi + 1)}{\chi - \chi_i + 1} = \frac{\epsilon_{\text{tot}}}{\epsilon_{\text{tot}} - \chi_i}$$

where we have introduced the layer susceptibility

$$\chi_i = \frac{1}{\epsilon_0} \frac{\Delta P_i}{E_{\text{ext}}}$$

As a result, we have written all the relevant quantities in terms of the local susceptibilities  $\chi_i$ , which is convenient at conceptual and practical levels. Conceptually,  $\chi_i$  is a quantity we expect to be positive in all cases, because an applied electric field will create dipoles parallel to it. This basic local response of the material is physically and intuitively clear, because it is free from the subtleties (associated to the long-range electrostatic effects encapsulated in the local depolarizing fields) that affect the dielectric constant. Practically,  $\chi_i$  is very easy to compute from a Monte Carlo simulation, whether by explicitly applying an electric field and calculating the change in local polarization or by directly inspecting the fluctuations of the local polarizations in absence of applied field. The latter approach can be viewed as a generalization of the method described in, for example, ref. 43; similar fluctuation formulas for ferroelectric nanostructures were introduced in refs 13, 45.

The layers labelled by  $i$  will typically correspond to actual PbTiO<sub>3</sub> and SrTiO<sub>3</sub> layers, but we could also further sub-divide our superlattice. For example, the above formulas formally allow us to consider contributions from the interfaces, or from different regions within a layer. This kind of subdivision was used to prepare Fig. 3e, in which maps of the dielectric constant as a function of position along the superlattice stacking direction are reported.

The dielectric susceptibility  $\chi_i$  of a layer  $i$  can be viewed as a direct average of the susceptibilities  $\chi_i(x, y)$  coming from different regions of the  $x$ - $y$  plane of the layer. Hence, we can use a representation as in Fig. 3f to determine which part of a given layer (domain walls or domains) contributes the most to  $\chi_i$ . It could be tempting to interpret the layer dielectric constant  $\epsilon_i$  as coming from a collection of parallel capacitors, which would formally allow us to map  $\epsilon_i(x, y)$ . However, such a construction implicitly assumes an equal potential drop across the individual capacitors within layer  $i$ , which seems in conflict with the inhomogeneous in-plane structure of our PbTiO<sub>3</sub> layers.

For the calculation of local polarizations, we evaluated the local dipole and cell volume from the atomic positions and Born effective charges. We computed dipoles centred on the A (Pb/Sr) and B (Ti) sites of the perovskite structure, by considering the weighted contributions of the surrounding atoms. Thus, for example, the dipole centred on a specific Ti cation was computed by adding up contributions from the Ti itself, the six neighbouring oxygens (each such contribution was divided by two, because each oxygen has two first-neighbour Ti cations) and the eight neighbouring A (Pb/Sr) cations (each such contribution was divided by eight, as each A cation has eight first-neighbour Ti cations).

**Relation between atomistic simulations and experiment.** As already mentioned, our model potentials for PbTiO<sub>3</sub>-SrTiO<sub>3</sub> superlattices are not expected to render quantitatively accurate results. The difficulties in reproducing the behaviour of the bulk compounds in a quantitative way are discussed in refs 24, 46, in which evidence is given of the challenge these materials pose to first-principles methods. The model deficiencies are best captured by the error in the obtained transition temperatures: the model for PbTiO<sub>3</sub> used here gives a value of  $440 \text{ K}$  when solved in bulk-like conditions, far below the experimental result of  $760 \text{ K}$ . Similarly, we do not expect our models to accurately capture the dielectric response of the SrTiO<sub>3</sub> layers in the superlattice, which tend to be stiffer than the experimental ones. Fortunately, beyond these quantitative inaccuracies, the qualitative behaviour of individually PbTiO<sub>3</sub> and SrTiO<sub>3</sub> obtained from our simulations, as well as that of the PbTiO<sub>3</sub>-SrTiO<sub>3</sub> superlattice, seem perfectly in line with experimental observations and physical soundness.

With regard to the results for the PbTiO<sub>3</sub>-SrTiO<sub>3</sub> system, our atomistic simulations predict a phase transition occurring in two steps: at a relatively high temperature ( $490 \text{ K}$ ), the  $c/a$  ratio of the PbTiO<sub>3</sub> layers clearly reflects the onset of local instantaneous ferroelectric order; then, at a lower temperature (about  $370 \text{ K}$ ), the static multidomain ferroelectric state freezes in. Thus, according to these simulations, the interval between  $370 \text{ K}$  and  $490 \text{ K}$  is characterized by strongly fluctuating ferroelectric domains. This result is likely to be affected by finite-size effects in our simulations; yet, given the very large separation of the two transition temperatures, and the easy and frequent domain rearrangements observed in our Monte Carlo simulations, we believe it should be taken seriously. Experimentally, preliminary measurements of the (5, 4)<sub>28</sub> PbTiO<sub>3</sub>-SrTiO<sub>3</sub> superlattice (Extended Data Fig. 6) indicate that the kink in the measured temperature dependence of the  $c/a$  ratio (usually assumed to mark the ferroelectric transition) occurs at a slightly higher



(about 50 K) temperature than the appearance of domain satellites in the diffuse scattering. A similar temperature difference has been noted in figure 3 of ref. 47 for a superlattice of a different composition. However, further investigation is needed to clarify the polarization structure in this temperature range.

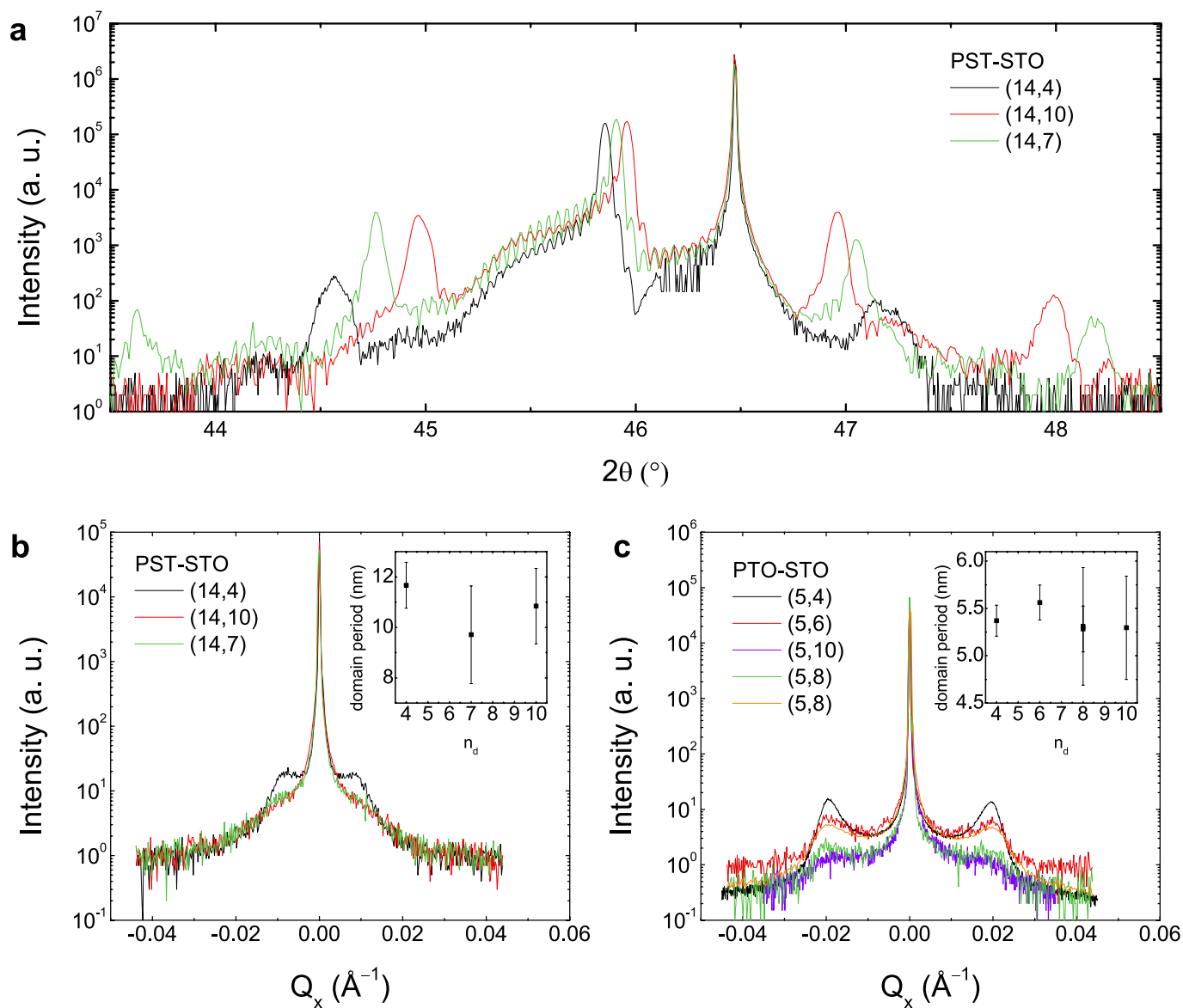
We also ran simulations of various  $(8, n_d)$  superlattices, and computed the corresponding total dielectric constants as a function of temperature, to mimic our experimental approach to estimate the response of the  $\text{PbTiO}_3$  layer. Extended Data Fig. 3 shows the results for  $\epsilon_f$  obtained in this way: we find a temperature interval in which the  $\text{PbTiO}_3$  layers present a negative dielectric constant, which validates our experimental strategy for estimating  $\epsilon_f$ .

If we compare the results in Extended Data Fig. 3 and Fig. 3c, then we note that the temperature interval in which the negative capacitance is observed is essentially the same, but the quantitative values for  $\epsilon_f$  clearly differ. Nevertheless, given the approximations involved in each of the two methods to compute  $\epsilon_f$ —for example, heuristic division into  $\text{PbTiO}_3$  and  $\text{SrTiO}_3$  layers and the implicit assumption that  $\text{PbTiO}_3$  layers in  $(8, n_d)$  superlattices of varying  $\text{SrTiO}_3$  content behave equivalently—these quantitative discrepancies do not seem very substantial and we have not investigated them further.

Finally, returning to our phenomenological predictions in Fig. 1c, it would appear that the Landau–Ginzburg result for the static domain structure bears a closer qualitative resemblance to the experimental data and the atomistic simulation results than does the Kittel model, despite the fact that it is the Kittel model that correctly captures the important contribution of domain-wall motion. However, in the Kittel model, we have not included the possibility of domain-wall pinning (by defects or otherwise), which would reduce the domain-wall contribution and could lead to an upturn of  $\epsilon_f$  at low temperatures. Quantifying the relative contributions to negative capacitance from domain-wall motion and the static domain response, both experimentally and through atomistic simulations, would be a worthwhile challenge for future studies.

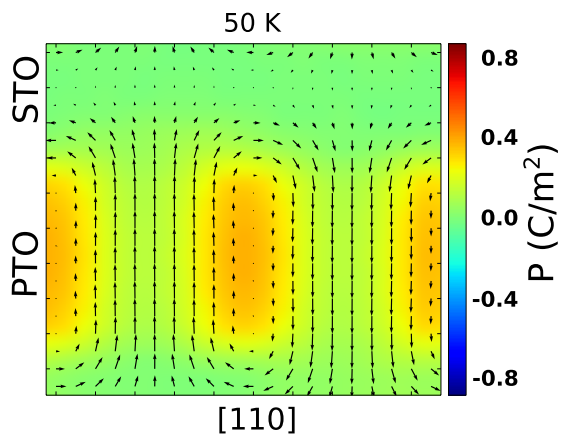
31. Landau, L. & Lifshits, E. On the theory of the dispersion of magnetic permeability in ferromagnetic bodies. *Phys. Zeitsch. Sow.* **8**, 153–169 (1935).

32. Kittel, C. Theory of the structure of ferromagnetic domains in films and small particles. *Phys. Rev.* **70**, 965–971 (1946).
33. Stephanovich, V. A., Luk'yanchuk, I. A. & Karkut, M. G. Domain-enhanced interlayer coupling in ferroelectric/paraelectric superlattices. *Phys. Rev. Lett.* **94**, 047601 (2005).
34. Catalan, G., Schilling, A., Scott, J. F. & Gregg, J. M. Domains in three-dimensional ferroelectric nanostructures: theory and experiment. *J. Phys. Condens. Matter* **19**, 132201 (2007).
35. Sené, A. *Theory of Domains and Nonuniform Textures in Ferroelectrics*. PhD thesis, Université de Picardie (2010).
36. Zubko, P. *et al.* Electrostatic coupling and local structural distortions at interfaces in ferroelectric/paraelectric superlattices. *Nano Lett.* **12**, 2846–2851 (2012).
37. Plonka, R., Dittmann, R., Pertsev, N. A., Vasco, E. & Waser, R. Impact of the top-electrode material on the permittivity of single-crystalline  $\text{Ba}_{0.7}\text{Sr}_{0.3}\text{TiO}_3$  thin films. *Appl. Phys. Lett.* **86**, 202908 (2005).
38. Stengel, M. & Spaldin, N. A. Origin of the dielectric dead layer in nanoscale capacitors. *Nature* **443**, 679–682 (2006).
39. Catalan, G., O'Neill, D., Bowman, R. M. & Gregg, J. M. Relaxor features in ferroelectric superlattices: a Maxwell–Wagner approach. *Appl. Phys. Lett.* **77**, 3078–3080 (2000).
40. Ghosez, P., Cockayne, E., Waghmare, U. V. & Rabe, K. M. Lattice dynamics of  $\text{BaTiO}_3$ ,  $\text{PbTiO}_3$ , and  $\text{PbZrO}_3$ : a comparative first-principles study. *Phys. Rev. B* **60**, 836–843 (1999).
41. Bousquet, E. *et al.* Improper ferroelectricity in perovskite oxide artificial superlattices. *Nature* **452**, 732–736 (2008).
42. Lisenkov, S. & Bellaiche, L. Phase diagrams of  $\text{BaTiO}_3/\text{SrTiO}_3$  superlattices from first principles. *Phys. Rev. B* **76**, 020102 (2007).
43. García, A. & Vanderbilt, D. Electromechanical behavior of  $\text{BaTiO}_3$  from first principles. *Appl. Phys. Lett.* **72**, 2981–2983 (1998).
44. Aguado-Puente, P. & Junquera, J. Structural and energetic properties of domains in  $\text{PbTiO}_3/\text{SrTiO}_3$  superlattices from first principles. *Phys. Rev. B* **85**, 184105 (2012).
45. Ponomareva, I., Bellaiche, L. & Resta, R. Relation between dielectric responses and polarization fluctuations in ferroelectric nanostructures. *Phys. Rev. B* **76**, 235403 (2007).
46. Wojdel, J. C. & Iñiguez, J. Testing simple predictors for the temperature of a structural phase transition. *Phys. Rev. B* **90**, 014105 (2014).
47. Zubko, P. *et al.* Ferroelectric domains in  $\text{PbTiO}_3/\text{SrTiO}_3$  superlattices. *Ferroelectrics* **433**, 127–137 (2012).



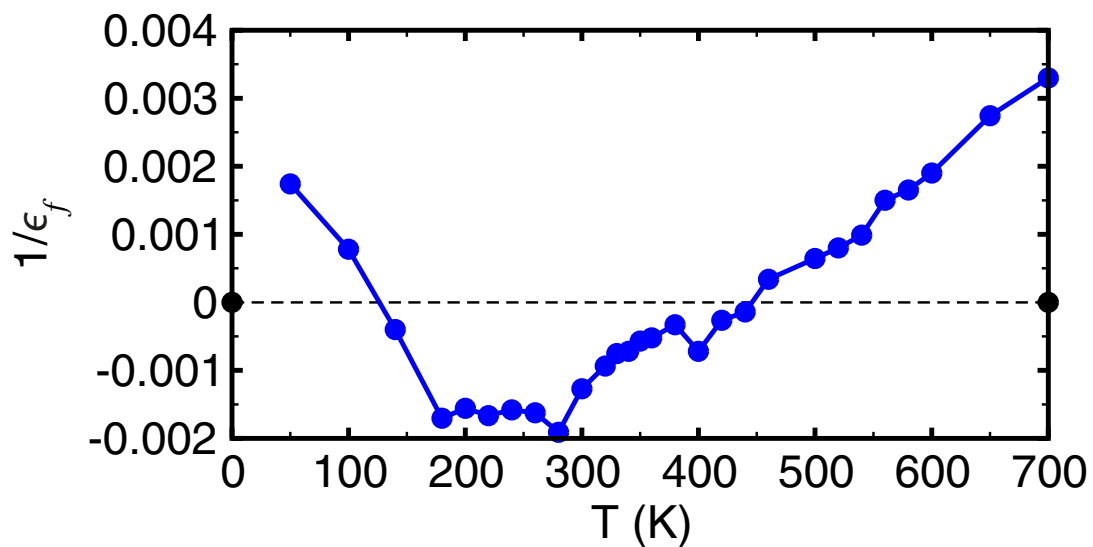
**Extended Data Figure 1 | XRD characterization of the superlattices.**  
**a**, Intensity profiles around the (002) substrate reflection for  $\text{Pb}_{0.5}\text{Sr}_{0.5}\text{TiO}_3$ - $\text{SrTiO}_3$  (PST-STO) superlattices. The broad peaks around  $2\theta = 45.5^\circ$  correspond to the top and bottom  $\text{SrRuO}_3$  electrodes. Finite-size oscillations due to the 200-nm superlattice thickness are visible. **b**, **c**, XRD domain satellites for  $\text{Pb}_{0.5}\text{Sr}_{0.5}\text{TiO}_3$ - $\text{SrTiO}_3$  (**b**) and  $\text{PbTiO}_3$ - $\text{SrTiO}_3$  (PTO-STO; **c**) superlattices. Insets, domain periodicities

obtained from fitting the  $Q_x$  line profiles using a sum of two Gaussian functions for the domain satellites and a Lorentzian function for central Bragg peak. The error bars were determined from the 95% confidence bounds for the peak positions obtained from the fits.  $n_d$  is the number of  $\text{SrTiO}_3$  layers in the (14,  $n_d$ ) (**b**) or (5,  $n_d$ ) (**c**) superlattices;  $Q_x$  is the in-plane reciprocal-space coordinate.

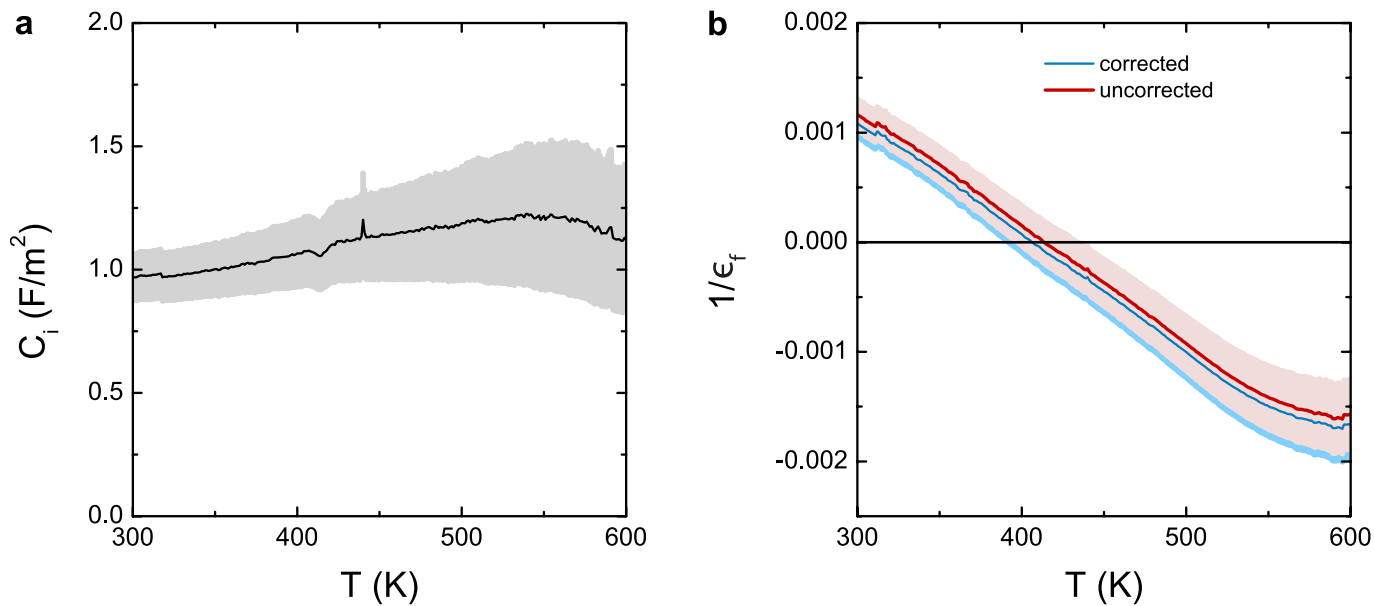


**Extended Data Figure 2 | Local polarization distribution at low temperature.** Arrows indicate the dipole component within the (110) plane; we plot arrows for Pb/Sr-centred and Ti-centred dipoles. The colouring indicates the polarization  $P$  component along  $[110]$ , revealing a low-temperature polar order at the domain walls. PTO, PbTiO<sub>3</sub>; STO, SrTiO<sub>3</sub>.

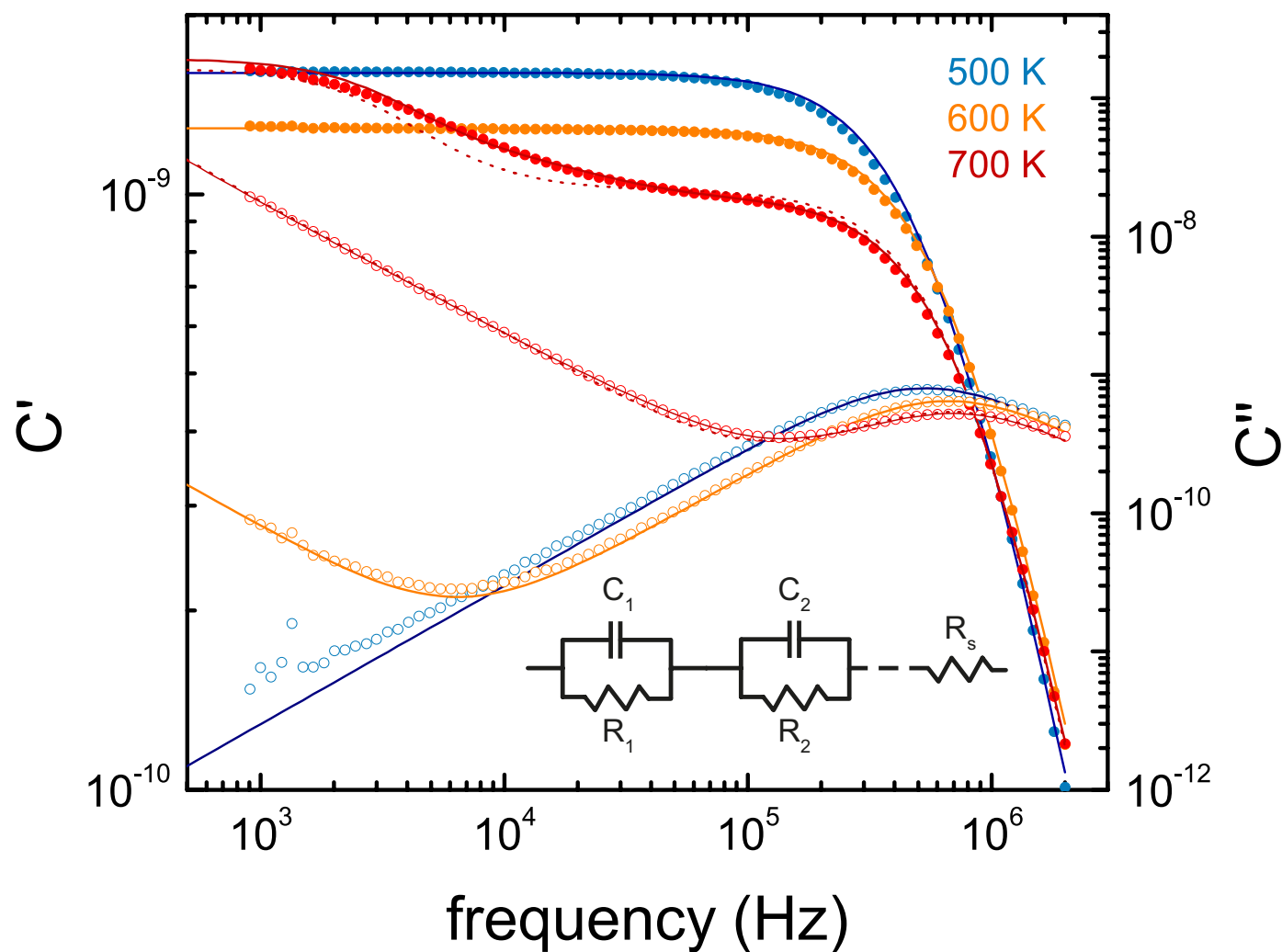




**Extended Data Figure 3 | Comparison with experiment.** Reciprocal dielectric constant  $1/\epsilon_f$  of the  $\text{PbTiO}_3$  layers as a function of temperature  $T$ , calculated from the computed total dielectric constants of  $(8, n_d)$  superlattices using the same analysis as for the experimental data.



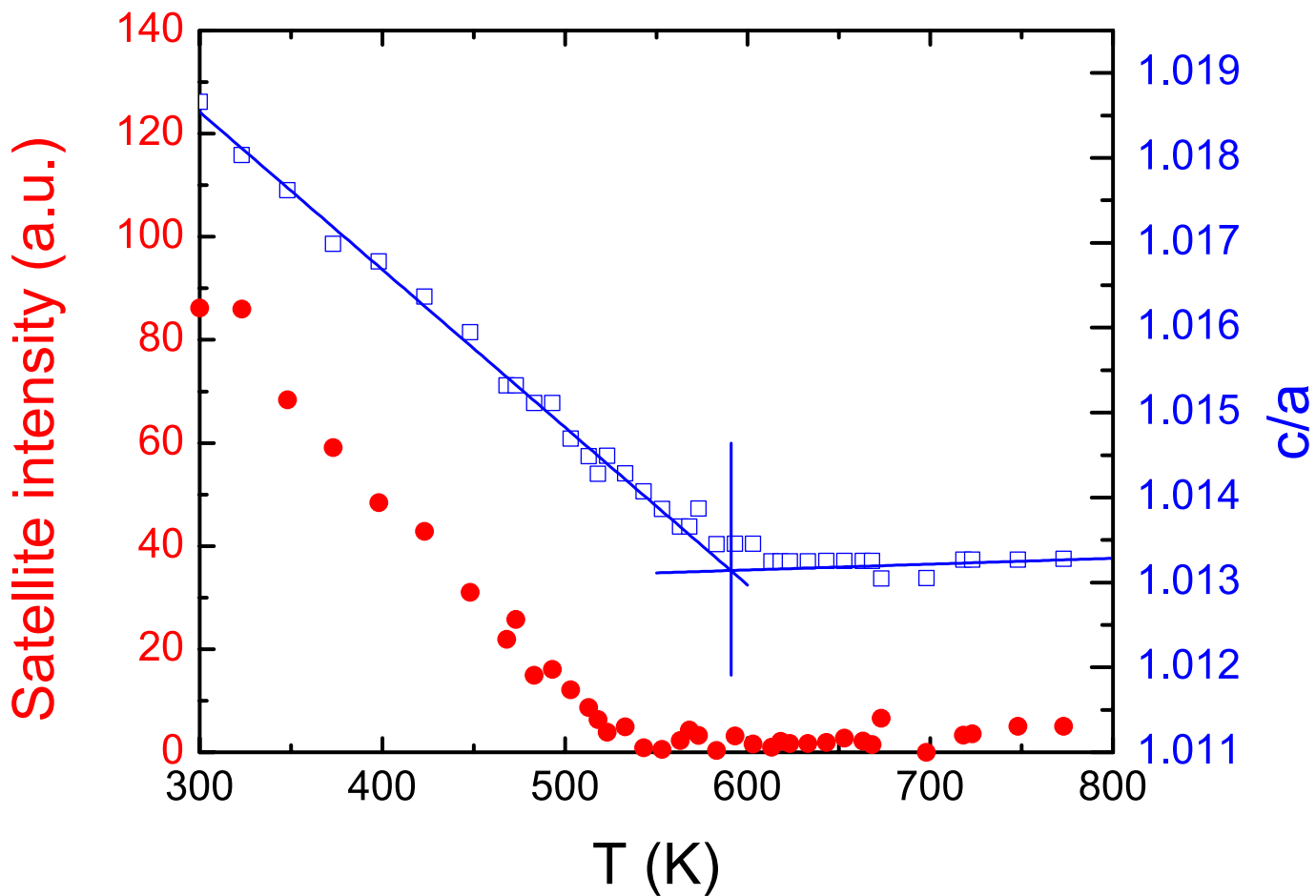
**Extended Data Figure 4 | Interface capacitance contributions.** **a**,  $\text{SrRuO}_3$ - $\text{SrTiO}_3$  interface contribution  $C_i$  to the dielectric response. **b**, Dielectric stiffness  $1/\epsilon_f$  of the  $\text{PbTiO}_3$  layers with (blue) and without (red) correcting for the interface capacitance. Grey (a) and blue and pink (b) shading indicates estimated uncertainties obtained from weighted-least-squares linear fits.



**Extended Data Figure 5 | Dielectric impedance spectroscopy of  $\text{PbTiO}_3$ - $\text{SrTiO}_3$  superlattices.** Real ( $C'$ ; filled circles) and imaginary ( $C''$ ; open circles) parts of the complex capacitance function  $C = C' + iC''$  for a  $(5, 8)_{30}$   $\text{PbTiO}_3$ - $\text{SrTiO}_3$  superlattice. For temperatures below about 650 K, the data are well fitted by a single parallel R-C element in series with  $R_s$ , as shown by solid curves for the 500 K (blue) and 600 K (orange) data. At higher temperatures, Maxwell-Wagner relaxations appear as the

conductivities of some layers increase faster with temperature than others. At 700 K (red), the response is qualitatively captured by a model with two parallel R-C elements in series with each other (dashed red curve), whereas for a quantitative fit three R-C elements are required (solid red curve). The inset shows the arrangement of elements in the generalized equivalent circuit used to fit the data.





**Extended Data Figure 6 | Temperature evolution of the tetragonality and domain satellites.** Intensity of the XRD domain satellite (filled red circles) and the film tetragonality ( $c/a$ ; open blue squares) for a  $(5, 4)_{28}$   $\text{PbTiO}_3$ - $\text{SrTiO}_3$  superlattice. The satellite intensity was obtained by

integrating the measured intensity of the domain satellites and subtracting the minimum integrated intensity in the paraelectric phase. Vertical blue line marks the temperature at which linear fits to the low- and high-temperature data (blue lines) intersect.